Effects of Radial Thermal Conduction and Radiation Transport During Fuel Pellet Implosion in Heavy-Ion Inertial Fusion*)

Naoto WATANABE, Kazumasa TAKAHASHI, Toru SASAKI and Takashi KIKUCHI

Nagaoka University of Technology, Nagaoka 940-2188, Japan

(Received 10 January 2022 / Accepted 6 May 2022)

We investigated the effects of radial thermal conduction and radiation transport from a fuel pre-heating for during the implosion process. We proposed a target structure using a Pb pusher to prevent the pre-heating phenomenon. We compared the electron heat and radiation fluxes, optical thickness, radiation temperature of the fuel, and fuel compression ratio for the Al and Pb pushers. For the Pb pusher, the compression ratio of the fuel increased when pre-heating was prevented. The results indicated that a pusher with a high-Z and dense material could minimize pre-heating and achieve a high fuel compression ratio. This is because such a material can maintain higher opacity during the implosion process.

Keywords: heavy-ion inertial fusion, implosion, pre-heating, radiation transport, thermal conduction

DOI: 10.1585/pfr.17.2404086

1. Introduction

Heavy-ion inertial fusion (HIF) is a promising candidate for future electric power generation because of its desirable properties, such as the high energy conversion efficiency and repetition rate capability of heavy-ion beams. A fuel should be compressed to one thousand times the solid density in the HIF system to obtain sufficient fusion output energy. The fuel pellet consists of a tamper layer, ablator layer, and fuel layer. The ablator layer expands and drives the implosion by absorbing the beam energy. The tamper layer is heavy and prevents the fuel pellet from expanding outward during the implosion process.

To realize a higher fuel compression ratio, the energy deposition by heavy-ion beam (HIB) irradiation is kept lower than a few percent because of non-uniformity. To solve this problem, a fuel target structure with a low-density layer has been proposed to mitigate the non-uniformity of radiation transport in the azimuthal direction [1, 2]. However, the radiation energy in the metal foam layer is also transported in the radial direction, which preheats the center of the fuel pellet; thus, the fuel compressibility required for sufficient fusion output cannot be obtained. While radial radiative transport causes energy transfer from the low-density layer to the center of the fuel pellet, the fuel is heated owing to thermal conduction by electrons during the implosion process. Therefore, it is expected to mitigate the fuel pre-heating that occurs during implosion by constraining the radial heat flux and radial radiation transport into the core of the fuel pellet. Subsequently, we proposed a novel concept for fuel pellets that use heavy materials in the pusher layer that can effectively block radial radiation transport.

In this study, we developed a one-dimensional radiation hydrodynamic code and investigated the effects of radial thermal conduction and radiation transport from a fuel pre-heating standpoint during the implosion process.

2. Calculation Model

Using a 1-D spherical coordinate radiative hydrodynamic model, we solved the hydrodynamic and radiation transport equations in lagrangian coordinate as follows:

$$\frac{Du_r}{Dt} = -\frac{1}{\rho}\frac{\partial}{\partial r}(P_i + P_e + P_r + q), \tag{1}$$

$$\rho C_{vi}\frac{DT_i}{Dt} = -(P_i + q)\left(\frac{1}{r^2}\frac{\partial(r^2u_r)}{\partial r}\right) - \frac{1}{r^2}\frac{\partial}{\partial r}(r^2F_i) - Q_{ei}, \tag{2}$$

$$\rho C_{ve}\frac{DT_e}{Dt} = -P_e\left(\frac{1}{r^2}\frac{\partial(r^2u_r)}{\partial r}\right) - \frac{1}{r^2}\frac{\partial}{\partial r}(r^2E_e) - Q_{er} + Q_{ei} + S_e, \tag{3}$$

$$\frac{DE_r}{Dt} = -P_r\left(\frac{1}{r^2}\frac{\partial(r^2u_r)}{\partial r}\right) + \frac{1}{r^2}\frac{\partial}{\partial r}(r^2F_r) + Q_{er}, \tag{4}$$

$$P_i = \frac{\rho}{m_uM}k_BT_i, \tag{5}$$

$$P_e = \frac{z^*\rho}{m_uM}k_BT_e\left(1 + \frac{2}{5}\frac{X\Theta^{-(y+1)} + Y\Theta^{-(y+1)/2}}{1 + X\Theta^{-y}}\right). \tag{6}$$

Here, ρ, u_r, T, E_r, and P are the mass density, velocity, temperature, radiation energy density, and pressure, respectively. The ideal gas fermion equation of state [3] is used to obtain the equation for state of the electrons in Eq. (6). q is an artificial viscosity term. C_{vi} and C_{ve} denote the ion- and electron-specific heats for a constant volume, respectively. Q_{ie} and Q_{re} are the energy exchange

author's e-mail: s195052@stn.nagaokaut.ac.jp

*) This article is based on the presentation at the 30th International Toki Conference on Plasma and Fusion Research (ITC30).

terms between the ion electron and radiation electron, respectively. F is the heat flux term [4]. S_e represents the source term of the electron from the stopping power. In this study, the stopping power is defined based on Bethe-Bloch and LSS theories for bound electrons [5]. The ionization state z^* is calculated using the Saha ionization equation [6]. m_u, M and k_B are the atomic mass constant, mass number and Boltzmann constant respectively. $\Theta = T_e/T_F$ is the normalized temperature and $X = 0.27232$, $Y = 0.145$ and $y = 1.044$. T_F is the Fermi temperature. The subscripts i, e, and r represent ions, electrons, and radiation, respectively.

3. Calculation Condition

Figure 1 illustrates the fuel target model. The fuel target structure is applied to that used in a previous study [1]. The fuel target consists of a tamper layer, ablator layer, foam layer, pusher layer, and fuel layer. The tamper layer is heavy and prevents the fuel pellet from expanding outward during the implosion process. The ablator layer expands and drives the implosion by absorbing the beam energy. The foam layer mitigates the non-uniformity of the deposition energy by propagating the radiation during the implosion process. The pusher layer prevents the preheating phenomenon and compresses the fuel [7]. Subsequently, in this study, two pusher layers, (a) Al and (b) Pb, were used for the calculations.

The Pb, Al, foam, and fuel (DT) layer mass densities are 11.3 g/cm^3, 2.69 g/cm^3, 0.13 g/cm^3, and 0.19 g/cm^3, respectively. The mass density of the foam layer is 0.05 times the Al solid density in this study. The thicknesses of the tamper, ablator, foam, pusher, and DT layers are 30, 430, 1000, 70, and 180 μm, respectively.

Figure 2 shows the HIB pulse waveforms. In this case, lead ions are used as the beam species, with foot pulses of 6 TW (6.2 ns) and 320 TW for the main pulse (9.2 ns).

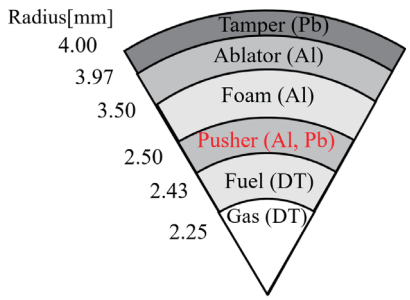

Fig. 1 Target structure with foam layer.

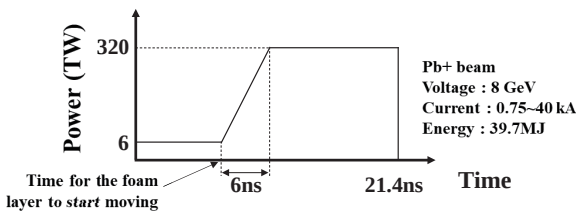

Fig. 2 HIB pulse waveform.

The transition from the foot pulse to the main pulse occurs when the foam layer begins to move. The pulse width during this transition is set to 6 ns. The total HIB energy is 3.97 MJ.

4. Calculation Results

Figure 3 shows the layer distributions during the implosion process of the targets for the (a) Al and (b) Pb pusher layers. The HIB incident on the tamper layer is absorbed in the ablator layer. The ablator layer drives the ablative shock inward. The compression wave from the ablation layer proceeds inward and reaches the DT fuel, causing the DT fuel to accelerate inward. Subsequently, the DT fuel is concentrated in the center, resulting in the compression of the fuel. However, the result presented in Fig. 3 (a) shows that the fuel is not adequately compressed compared to the result presented in Fig. 3 (b). The fuel layer suddenly decelerated near the center of the sphere owing to the pressure increase during implosion. For this reason, the fuel was not adequately compressed. This phenomenon was attributed to radial heat transport pre-heating in the fuel layer.

5. Effect of Radiation and Electron Heat Fluxes

Figure 4 shows the fluxes in the inner pusher layers: (a) the electron heat flux and (b) the radiation flux. The fluxes are defined as follows:

$$F_r = -\frac{c\lambda}{\sigma_R}\frac{\partial E_r}{\partial r}, \tag{7}$$

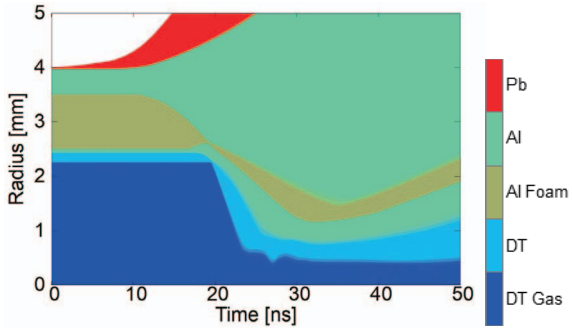

(a) Al pusher

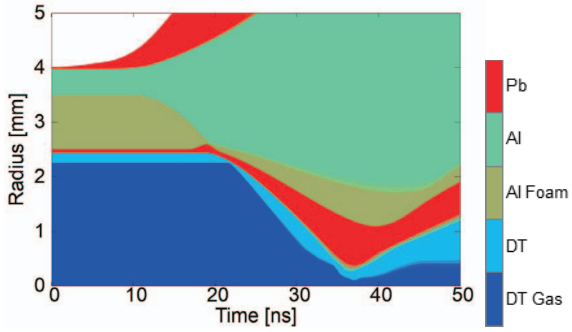

(b) Pb pusher

Fig. 3 Material distribution of a target during the implosion process.

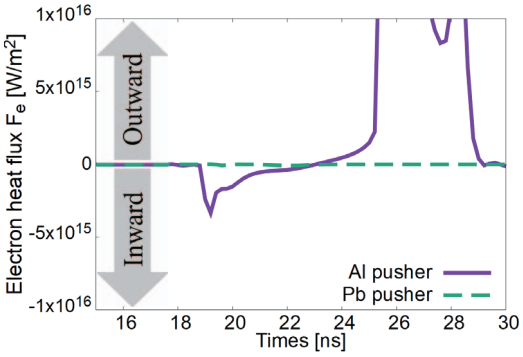

(a) Electron heat flux

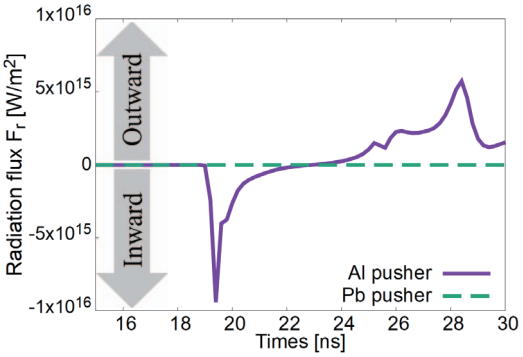

(b) Radiation flux

Fig. 4 Fluxes in inner layer of pusher during implosion process.

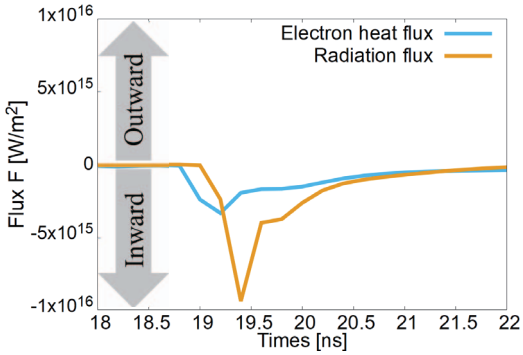

Fig. 5 Electron heat and radiation fluxes at interface between the fuel and pusher during the implosion process.

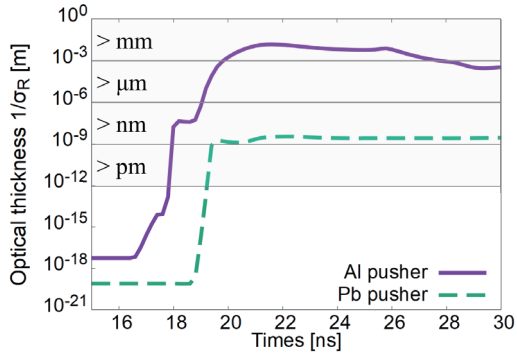

Fig. 6 Optical thickness at interface between the fuel and pusher during the implosion process.

$$F_e = -\kappa_e \frac{\partial T_e}{\partial r}. \tag{8}$$

Here, c, λ, σ_R and κ_e are the speed of light, flux limiter, Rosseland mean opacity and electron hear conduction coefficient respectively. Because the ion heat flux is significantly lower than the radiation and electron heat fluxes, only the radiation and electron heat fluxes are considered in the comparison.

As shown in Fig. 4, a positive flux value indicates an outward energy transfer, while a negative flux indicates an inward energy transfer. In Fig. 4, inward fluxes for electrons and radiation can be observed inside the Al pusher. However, neither the electron heat flux nor radiation heat flux can be observed in the Pb pusher. Therefore, the discussion on the fluxes will focus on the results obtained with the Al pusher.

Figure 5 illustrates the radiation and electron heat fluxes at the inner boundary of the Al pusher. The electron heat flux in the inward direction increases before the radiation flux does. The results indicate that the pusher layer is heated by electron thermal conduction and becomes optically thin owing to the thermal expansion of the pusher layer and increase in the electron temperature. Consequently, the radiation flux propagated inward from the ablator and foam layers through the pusher layer. Because the radiation flux is larger than the electron heat flux, we assume that the heating of the fuel was dominated by radiative transport. Therefore, it is important to evaluate the optical thickness of the inner pusher layer during the implosion process.

Figure 6 shows the optical thickness at the interface between the fuel and pusher. The opacity is estimated as follows [8]:

$$\sigma_R = 1.4 \frac{Z^3}{M^2} \rho^2 T_e^{-7/2} \ [1/\mathrm{m}]. \tag{9}$$

Here, Z is atomic number. This shows that the optical thickness at the fuel and pusher interface increases as the implosion progresses. The optical thickness of the Al pusher increases in the order of millimeters. Because the initial pusher layer thickness was 70 μm, the optical thickness is sufficiently larger than that of the Al pusher. Consequently, the radiation flux can pass through the pusher layer to the fuel. On the other hand, for the Pb pusher, the optical thickness during the implosion process is in the order of nanometers and sufficiently smaller than that of the Pb pusher. Therefore, we assume that the Pb pusher prevents the radiation transport into the fuel.

6. Effect of Pre-Heating

Figure 7 shows the radiation temperature in the fuel layer as a function of time normalized by the time at which the minimum fuel layer radius occurs in the Al and Pb pushers. In Fig. 7, the temperature rise can be observed before the time at which the minimum fuel layer radius oc-

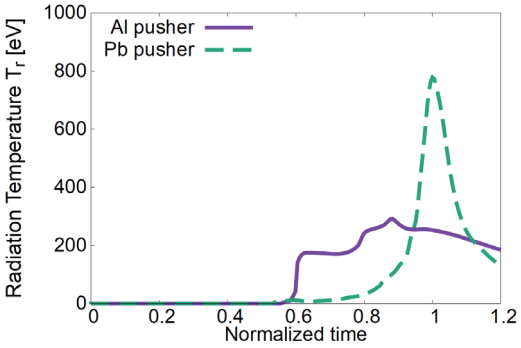

Fig. 7 Fuel radiation temperature during the implosion process.

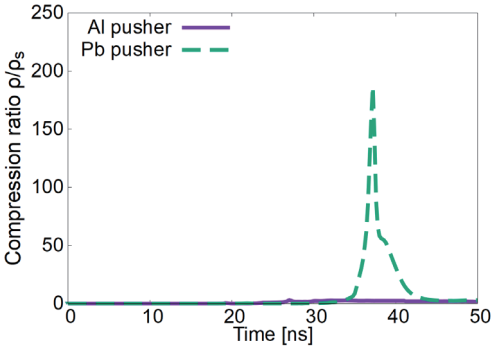

Fig. 8 Fuel compression ratio during the implosion process.

curs, indicating that the radiation energy propagates to the fuel. For this reason, the fuel is pre-heated owing to radiation flux. For the Pb pusher, the radiation temperature increases before the time at which the minimum fuel layer radius is smaller than that for the Al pusher. This implies that the Pb pusher interferes with the pre-heating of fuel, contrarily to the Al pusher. These results are consistent with the heat flux and optical thickness results, as indicated in the previous section, and show that using a high-Z material with high density and sufficient optical pusher layer thickness can prevent the radiation transport from the foam layer to the fuel layer.

Figure 8 shows the fuel compression ratios of the target for the Al and Pb pushers. As shown in Fig. 8, a high compression ratio cannot be obtained for the Al pusher. This is attributed to the pre-heating caused by both the radiation transport and electron thermal conduction considering the discussions stated above. On the other hand, a high compression ratio is obtained in the case of the Pb pusher because pre-heating is effectively prevented.

Figure 9 shows the results of the fuel compression ratio obtained by varying the thickness of each pusher and calculating the change in the pusher mass. Observe that the fuel compression ratio increases as the pusher mass increases. In the case of the Pb pusher, the fuel can be compressed approximately 200 times. From these figures, observe that the maximum compression ratio of the Pb pusher is 17 times greater than that of the Al pusher.

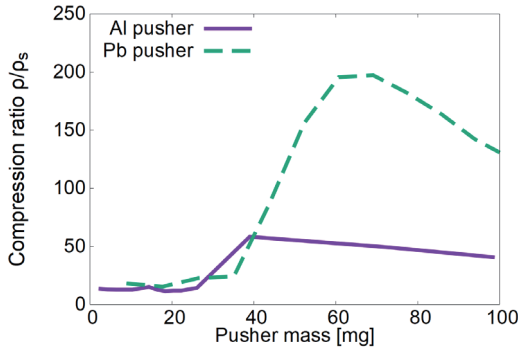

Fig. 9 Compression ratio of fuel with respect to pusher mass.

7. Conclusion

In this study, we developed a one-dimensional radiation hydrodynamic code and investigated the effects of radial thermal conduction and radiation transport considering the fuel pre-heating phenomenon during the implosion process.

To prevent pre-heating, we proposed a target structure using a Pb pusher, in which the electron heat and radiation fluxes, optical thickness, fuel radiation temperature, and fuel compression ratio were compared with those for an Al pusher.

Based on the calculation results, in the case of the Al pusher, a higher compression ratio could not be obtained because of the pre-heating caused by both radiation transport and electron thermal conduction. On the other hand, in the case of the Pb pusher, a high compression ratio was obtained because pre-heating was effectively prevented. The results indicated that a pusher with a high-Z and dense material could minimize pre-heating and achieve a high fuel compression ratio. This is because the proposed material can maintain higher opacity during the implosion process.

[1] T. Someya, K. Miyazawa, T. Kikuchi and S. Kawata, "Direct-indirect mixture implosion in heavy ion fusion", Laser Part. Beams **24**, 359 (2006).
[2] S. Kawata, T. Karino and A.I. Ogoyski, "Review of heavy-ion inertial fusion physics", Matter Radiat. Extremes **1**, 89 (2016).
[3] S. Ichimaru, Statistical Plasma Physics II: Condensed Plasmas (Westview Press, 2004), p.185 and in Appendix B.
[4] J.P. Christiansen, D.E.T.F. Ashby and K.V. Roberts, "MEDUSA a one-dimensional laser fusion code", Comput. Phys. Commun. **7**, 271 (1974).
[5] T.A. Mehlhorn, "A finite material temperature model for ion energy deposition in ion-driven inertial confinement fusion targets", J. Appl. Phys. **52**, 6522 (1981).
[6] J.W. Fowler, "Saha Equation Normalized to Total Atomic Number Density", Solar and Stellar Astrophysics. arXiv: 1209.1111
[7] D.S. Montgomery *et al.*, "Design considerations for indirectly driven double shell capsules", Phys. Plasmas **25**, 092706 (2018).
[8] S. Atzeni and J. Meyer-ter-Vehn, "The physics of inertial fusion: beam plasma interaction, hydrodynamics, hot dense matter", **125** (Oxford University Press, Oxford, 2004).